Chem Soc Rev

Heavily-Doped Colloidal Semiconductor and Metal Oxide Nanocrystals: An Emerging New Class of Plasmonic Nanomaterials

Journal:	*Chemical Society Reviews*
Manuscript ID:	CS-TRV-11-2013-060417.R1
Article Type:	Tutorial Review
Date Submitted by the Author:	21-Jan-2014
Complete List of Authors:	Liu, Xin; University at Buffalo (SUNY), Chemical and Biological Engineering Swihart, Mark T.; University at Buffalo (SUNY), Department of Chemical and Biological Engineering;

Cite this: DOI: 10.1039/c0xx00000x

www.rsc.org/xxxxxx

ARTICLE TYPE

Heavily-Doped Colloidal Semiconductor and Metal Oxide Nanocrystals: An Emerging New Class of Plasmonic Nanomaterials

Xin Liu and Mark T. Swihart

Received (in XXX, XXX) Xth XXXXXXXXX 20XX, Accepted Xth XXXXXXXXX 20XX

DOI: 10.1039/b000000x

The creation and study of non-metallic nanomaterials that exhibit localized surface plasmon resonance (LSPR) interactions with light is a rapidly growing field of research. These doped nanocrystals, mainly self-doped semiconductor nanocrystals (NCs) and extrinsically-doped metal oxide NCs, have extremely high concentrations of free charge carriers, which allows them to exhibit LSPR at near infrared (NIR) wavelengths. In this tutorial review, we discuss recent progress in developing and synthesizing doped semiconductor and metal oxide nanocrystals with LSPR, and in studying the optical properties of these plasmonic nanocrystals. We go on to discuss their growing potential for advancing biomedical and optoelectronic applications.

Key learning points

(1) Localized surface plasmon resonance (LSPR) has been demonstrated in several types of heavily-doped colloidal semiconductor and metal oxide nanocrystals.

(2) Nanocrystals exhibiting LSPR can be classified as intrinsically-doped or extrinsically-doped.

(3) Lower free carrier concentrations in plasmonic semiconductor NCs, compared to noble metals, produce LSPR at longer wavelengths.

(4) Plasmonic semiconductor NCs have particularly high potential for biomedical applications in which strong NIR absorbers are needed.

(5) Potential applications of these nanocrystals are also emerging in photonics, optoelectronics, and nanoelectronics.

1. Introduction

With the rapid development of nanotechnology, many classes of nanomaterials with unique physical and chemical properties have been created and are beginning to be used in practical applications. Among the unique phenomena observed in nanoscale materials, surface plasmon resonance (SPR)[1] and localized surface plasmon resonance (LSPR)[1] are particularly important optical properties that are increasingly playing important roles in theranostics,[2] nanophotonics[3] and nanoelectronics.[3] LSPR is commonly observed in noble metal nanostructures. It arises from the resonant interaction of their free electrons with the oscillating electromagnetic field of light. The first scientific reports on synthesis and optical properties of metal nanostructures, specifically colloidal gold, were made by Faraday more than 150 years ago.[4] Progress in this field accelerated dramatically over the past two decades, and many methods for synthesizing noble metal nanostructures with well-defined morphology and uniform size have been developed.[2, 5, 6] Gold (Au) nanostructures are the most systematically investigated, due to their chemical inertness and relative synthetic accessibility. Spherical gold nanoparticles from about 3 to 50 nm in diameter exhibit LSPR at visible wavelengths. Hollow or anisotropic gold nanostructures can exhibit multiple LSPR modes over visible to near infrared (NIR) wavelengths.[2] Anisotropic structures (e.g. nanorods) can support multiple LSPR modes along different axes of the nanostructure.[5, 6] In hollow nanostructures (e.g. in nanoshells) plasmons at the inner and outer surface can couple to produce LSPR at longer wavelength. Such NIR absorbance is extremely useful for theranostic applications such as photothermal therapy (PTT) and bio-imaging, because the interaction of tissue with light at these wavelengths is relatively weak.[2]

Excitation of LSPR fundamentally relies on the interaction between free charge carriers and light.[1] Noble metal nanostructures exhibit this strong light-matter interaction due to their high density of free electrons. In the past five years, LSPR has been observed in heavily-doped semiconductor and metal oxide nanocrytals (NCs), where it is attributed to the high density of free charge carriers introduced by doping. Generation of free charge carriers in colloidal semiconductor or metal oxide NCs mainly involves two different doping pathways: (i) “intrinsic” formation of cation vacancies, also called self-doping, and (ii) “extrinsic” substitutional doping with heterovalent dopant atoms, also called exotic-doping. The density of free charge carriers achievable in

these doped NCs is lower than that of noble metals and, as a result, their LSPR is at lower energy or longer wavelength. The chemical synthesis of these new plasmonic nanomaterials, fundamental studies of their photophysics, and exploration of their applications in theranostics, nanophotonics and nanoelectronics are rapidly emerging research fields.

The origins and underlying physics of LSPR in nanoparticles of noble metals and heavily-doped semiconductors are the same – a resonant interaction of free charge carriers with the oscillating electromagnetic field of light. However, the systems differ in important practical respects. In particular, the charge carriers in noble metals are electrons, while in heavily-doped semiconductor or metal oxide NCs the free charge carriers can be electrons or holes. The LSPR frequency depends upon the density of free charge carriers, the charge carrier effective mass, and geometric factors. Heavily-doped semiconductor and metal oxide NCs generally have lower density of free charge carriers than noble metal NPs, and as a result exhibit lower energy (longer-wavelength) LSPR. Moreover, in heavily-doped semiconductors, the density of free charge carriers can vary with changes in degree of doping or even with changes in surface ligands. In metals, this is not possible; for a given metal, the charge carrier density is nearly fixed. In what follows, we mainly focus on the influence of the density of free charge carriers on the LSPR frequency of doped NCs, as this is the parameter most strongly affecting the LSPR wavelength.

In this tutorial review, we provide a comprehensive overview of progress in this rapidly expanding research field. We classify these plasmonic semiconductor nanomaterials as (1) intrinsically-doped NCs, which are mainly colloidal self-doped copper chalcogenide NCs, and (2) extrinsically-doped NCs, mainly consisting of indium tin oxide (ITO), aluminium doped zinc oxide (AZO), doped silicon (Si) and other doped metal oxide NCs. We review chemical methods for tuning LSPR in these NCs, which include stepwise reaction, *in situ* control during synthesis, and adjustment of LSPR by combining two types of plasmonic colloidal NCs. Finally, we discuss progress toward application of these new types of plasmonic nanomaterials in biomedical, electrochromic and optoelectronic fields.

2. Self-doped copper chalcogenide colloidal NCs with LSPR

In plasmonic semiconductor nanostructures, the free charge carriers responsible for LSPR can be either electrons or holes, depending upon the nature of the dopants. In this section, we focus on a group of doped semiconductor NCs in which free holes result from the presence of cation vacancies. These are often called self-doping or self-doped NCs. These intrinsically-doped materials are mainly copper-deficient copper chalcogenide NCs, including copper sulfide ($Cu_{2-x}S$), copper selenide ($Cu_{2-x}Se$), copper telluride ($Cu_{2-x}Te$) and the related alloy NCs. Here, we summarize advances in chemical synthesis of these materials and studies of LSPR in them.

2.1 $Cu_{2-x}S$ colloidal NCs with LSPR

LSPR is not observed in stoichiometric Cu_2S NCs due to the absence of free charge carriers. Despite many earlier papers on the synthesis and characterization of copper sulfide NCs, the NIR LSPR in copper-deficient $Cu_{2-x}S$ NCs was first observed and identified as plasmonic absorbance by Zhao et al. in 2009.[7] They proposed that the free charges in $Cu_{2-x}S$ NCs are free holes associated with cation vacancies. Upon increasing the degree of copper deficiency, the plasmonic resonance peak shifts to higher frequency (i.e., blue shifts). The LSPR frequency is correlated with the charge carrier density in the NCs, as shown in **Fig. 1**. Luther et al. developed a method to synthesize colloidal dispersions of monodisperse $Cu_{2-x}S$ NCs.[8] The density of the free holes in the self-doped $Cu_{2-x}S$ NCs was estimated to be near ~2×10^{21} cm^{-3}, corresponding to a LSPR frequency in the mid-IR to NIR spectral region.

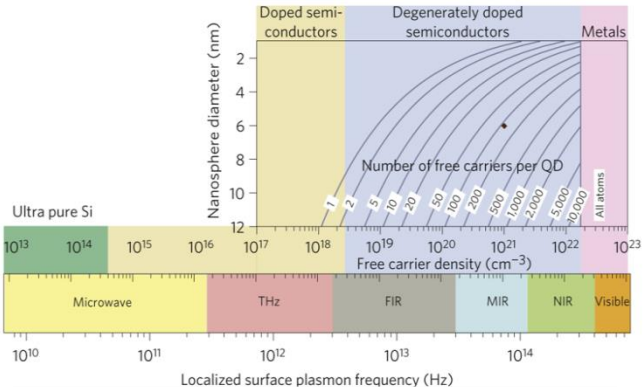

Fig. 1 Dependence of localized surface plasmon resonance frequency on the density of free carriers. Reproduced with permission from Luther et al.[8] Copyright © 2011 Nature Publishing Group.

In the classical Drude model, charge carriers are treated as a system of non-interacting "quasi-particles" that move freely within the material, interacting with the lattice of nuclei only through instantaneous collisions. It provides a relatively simple basis for understanding the LSPR phenomenon and relating LSPR energy to the free carrier density.[1] Equation 1 shows the Drude model for the dielectric function of a material with free charge carriers. The dielectric function is composed of a real part (ε_1) and an imaginary part (ε_2), i.e. $\varepsilon(\omega) = \varepsilon_1(\omega) + i\varepsilon_2(\omega)$. In Eq. (1), ω_p is the bulk plasmon frequency, γ is a damping frequency, reflecting the plasmon bandwidth, n is the density of free charge carriers, e is the charge of the electron, ε_0 is the vacuum permittivity and m_{eff} is the effective mass of the charge carriers (electrons or holes). In cation-deficient copper chalcogenides, the free charge carriers are holes that arise from copper deficiency. Note that interband transition or excitonic transition terms are not included in this model. The real part of the dielectric function is shown in equation (2), obtained by simplifying equation (1). The polarizability (α) of a sub-wavelength nanoparticle is described by the Clausius–Mossotti relation[1,8] shown in (3), where V is the volume of the NP and ε_m is the dielectric constant of the surrounding medium in which the NPs are dispersed. The polarizability exhibits a resonant

$$\boldsymbol{\varepsilon(\omega) = 1 - \frac{\omega_p^2}{\omega(\omega+i\gamma)}, \omega_p^2 = \frac{ne^2}{\varepsilon_0 m_{\text{eff}}}} \quad \textbf{(1)}$$

$$\boldsymbol{\varepsilon_1(\omega) = 1 - \frac{\omega_p^2}{\omega^2+\gamma^2}, \varepsilon_2(\omega) = \frac{\omega_p^2\gamma}{\omega(\omega^2+\gamma^2)}} \quad \textbf{(2)}$$

$$\boldsymbol{\alpha = 3\varepsilon_0 V \frac{\varepsilon(\omega)-\varepsilon_m}{\varepsilon(\omega)+2\varepsilon_m}} \quad \textbf{(3)}$$

$$\boldsymbol{\alpha_i = 3\varepsilon_0 V \frac{\varepsilon(\omega)-\varepsilon_m}{3\varepsilon_m+3L_i(\varepsilon(\omega)-\varepsilon_m)}} \quad \textbf{(4)}$$

enhancement when the denominator in Eq. (3) approaches zero, i.e. when $\varepsilon_1(\omega) = -2\varepsilon_m$, provided that the imaginary component of the dielectric function, $\varepsilon_2(\omega)$ has weak frequency dependence. Based on the Drude model, the concentration of free holes in $Cu_{2-x}S$ NCs can be estimated from the peak LSPR absorbance wavelength and correlated with the copper deficiency (x).[8] In principle, one can simply work backward from setting the denominator of Eq. (3) equal to zero, using Eq. (1) for the frequency-dependent dielectric function. However, factors including the polydispersity of NCs and non-uniform elemental distribution may limit the applicability of this simple analysis. The damping frequency, γ, must be estimated from the width of the LSPR absorbance, and the effective mass of the carriers may not be known. This quasistatic approximation can also be applied to ellipsoidal and spheroidal shapes, such as $Cu_{2-x}S$ nanodisks,[9] by including a shape factor in the equations. Equation (4) shows the polarizabilities, α_i, along the different axes (i = 1,2,3) in ellipsoidal coordinates, where L_i is a geometrical factor. $Cu_{2-x}S$ nanodisks exhibited two LSPR peaks, attributed to the in-plane and out-of-plane plasmon modes, respectively, which is consistent with the prediction of the Drude model described above.

Several chemical methods including organic-phase synthesis, hydrothermal synthesis and sonoelectrochemical synthesis have been developed for preparing colloidal $Cu_{2-x}S$ NCs with appreciable copper deficiency, in addition to the many protocols developed for synthesizing stoichiometric or near-stoichiometric Cu_2S NCs. Monodisperse $Cu_{2-x}S$ quantum dots (QDs) 2.4, 3.6, and 5.8 nm in average diameter were prepared by reacting copper(II) acetylacetonate with ammonium diethyldithiocarbamate in the presence of dodecanethiol (DDT) and oleic acid (OA).[8] $Cu_{2-x}S$ NCs with an elemental composition of $Cu_{1.93}S$ exhibited a LSPR absorbance peak around 0.69 eV (~1800 nm wavelength, **Fig. 2A**). $Cu_{2-x}S$ nanodisks[9] were synthesized by combustion of copper alkanethiolate precursor which was prepared by reacting copper nitrate with dodecanethiol. The $Cu_{2-x}S$ nanodisks exhibit two plasmonic bands attributed to in-plane and out-of-plane modes, respectively (**Fig. 2B**). Because these methods were originally developed for synthesis of stoichiometric Cu_2S NCs, they produce $Cu_{2-x}S$ NCs with relatively low copper deficiency (small x) and corresponding low LSPR energy. A reaction model was later developed specifically to synthesize high-quality $Cu_{2-x}S$ NCs with greater copper deficiency, and therefore strong LSPR at higher energy.[10] The copper precursor was made by dissolving copper(I) chloride (CuCl) in coordinating solvents, oleylamine (OAm) or a mixture of OAm and oleic acid (OA). The sulfur precursor was

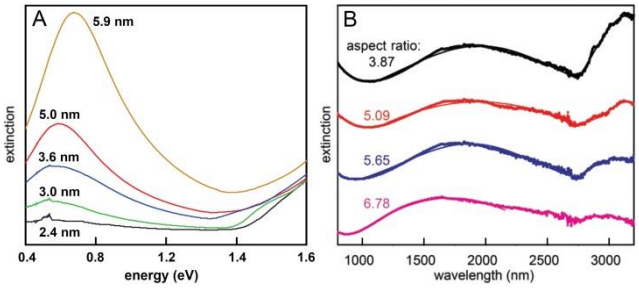

Fig. 2 (A) The evolution of LSPR energy with increasing size of $Cu_{2-x}S$ NCs. Adapted from Luther et al.[8] Copyright © 2011 Nature Publishing Group, (B) LSPR in disk-shaped $Cu_{2-x}S$ NCs, showing two plasmon modes whose positions depend upon the aspect ratio of the nanodisks. Adapted from Hsu et al.[9] Copyright © 2011 ACS

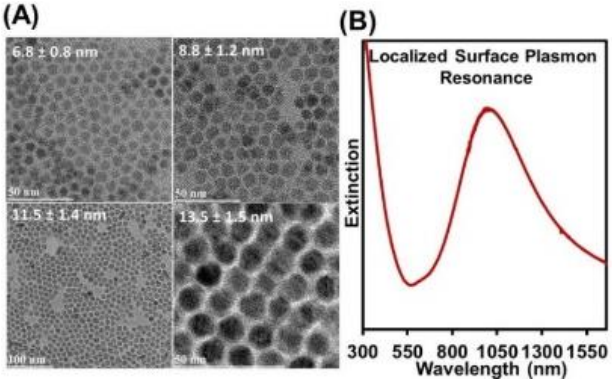

Fig. 3 (A) Transmission electron microscopy (TEM) images of $Cu_{2-x}S$ NCs with average sizes of 6.8, 8.8, 11.5, and 13.5 nm, respectively. Adapted from Liu et al.[10] Copyright © 2013 Wiley VCH, (B) LSPR in $Cu_{2-x}S$ NCs synthesized using CuCl-OAm and OA-S as the precursors show a sharp peak centered at 975 nm. Adapted from Liu et al.[11] Copyright © 2013 ACS Publications.

also prepared by reacting sulfur powder with coordinating solvents, including OAm and OA.[10] Monodisperse $Cu_{2-x}S$ NCs with controllable and tunable size were synthesized by varying the reaction conditions, particularly reaction temperature and the aging time for crystal growth. The resulting $Cu_{2-x}S$ NCs can exhibit an LSPR absorbance peak at wavelengths as short as 975 nm,[11] because this synthesis method can produce large copper deficiency, up to $x \approx 1$ (**Fig. 3**). This progress in synthesis of $Cu_{2-x}S$ NCs with plasmonic absorbance over the spectral region from 800 nm to 1200 nm favors development of biomedical applications, as specifically discussed in **section 5**.

2.2 $Cu_{2-x}Se$ colloidal NCs with LSPR

Cu_2Se has been studied as an absorber in photovoltaic devices because its band gap (1.1 eV-1.5 eV) is well matched to the solar spectrum. To synthesize Cu_2Se NCs, an organo-selenium precursor is typically prepared by dissolving Se powder in trioctylphosphine (TOP) or tributylphosphine (TBP).[12] Stoichiometric Cu_2Se NCs synthesized using TOP-Cu and TOP-Se as the precursors show negligible LSPR. Their absorbance at NIR wavelengths increased slightly after exposing the Cu_2Se NCs to the air for 1 day, but did not show obvious additional changes upon further air exposure for up to 2 weeks.[12] The emergence of NIR absorbance following air exposure can be attributed to LSPR that, in turn, results from copper deficiency arising from oxidation of Cu_2Se NCs in air. However, the LPSR in these lightly-doped $Cu_{2-x}Se$ NCs is weak compared with that of $Cu_{2-x}Se$ NCs directly synthesized with large copper deficiency.

High-quality $Cu_{2-x}Se$ NCs with significant cation vacancy were produced using a phosphine-free reaction system. Three types of phosphine-free selenium precursors including octadecene (ODE)-Se,[13] OAm-Se[10] and OA-Se[10] were produced by dissolving Se powder in ODE, OAm and OA, respectively. Copper precursors were prepared by dissolving inorganic copper halides in coordinating ligands/solvents. Nucleation was initiated at appropriate temperature followed by aging the colloidal dispersion for a time optimized for growing $Cu_{2-x}Se$ NCs. Deka et al. synthesized monodisperse $Cu_{2-x}Se$ NCs with a hexagonal shape using ODE-Se precursor (**Fig. 4**).[13] The $Cu_{2-x}Se$ NCs synthesized using ODE-Se are composed of a primary berzelianite crystal phase and a smaller fraction of a hexagonal crystal phase.

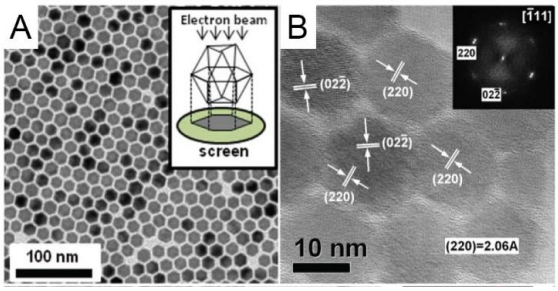

Fig. 4 (a) TEM image of ~16 nm $Cu_{2-x}Se$ NCs synthesized using ODE-Se precursor. (b) HRTEM and selected area electron diffraction (SAED) pattern of $Cu_{2-x}Se$ NCs. Adapted from Deka et al.[13] Copyright © 2010 ACS Publications.

Moreover, using the ODE-Se precursor, $Cu_{2-x}Se$ nanocubes could be obtained in the presence of Al ions.[14] OAm-Se and OA-Se precursors were studied for synthesizing monodisperse $Cu_{2-x}Se$ NCs with tunable size.[10] The nucleation and NC growth were investigated by combining experimental results and a theoretical model. The average size of $Cu_{2-x}Se$ NCs was tuned from ~6.2 to ~16.5 nm (**Fig. 5A, B, C&D**). Mixed crystal phases were observed in the $Cu_{2-x}Se$ NCs synthesized using OAm-Se precursor, while pure berzelianite crystal phase was obtained using OA-Se precursor. The $Cu_{2-x}Se$ NCs synthesized using these phosphine-free Se precursors all exhibited strong LSPR at higher energy (**Fig. 5E**) than that in $Cu_{2-x}Se$ NCs with nearly perfect stoichiometry or $Cu_{2-x}Se$ NCs obtained by slightly oxidizing Cu_2Se NCs in air. Moreover, a red-shift in the LSPR of $Cu_{2-x}Se$ NCs was observed with increasing concentration of OA employed in the synthesis. Further details of this method for tuning LSPR in $Cu_{2-x}Se$ NCs are discussed in **section 3.2**.

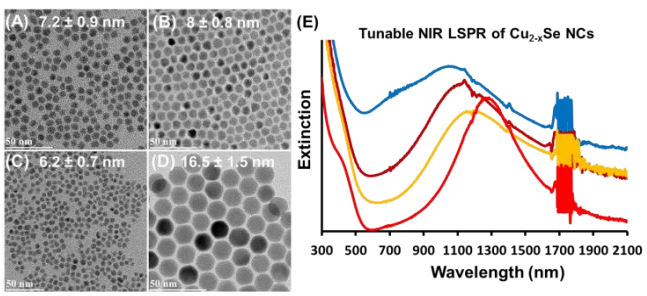

Fig. 5 (A), (B), (C) and (D) representative TEM images of $Cu_{2-x}Se$ NCs with mean size ~7.2 nm, ~8 nm, ~6.2 nm and ~16.5 nm synthesized using OAm-Se and OA-Se precursors. (E) Tunable LSPR in $Cu_{2-x}Se$ NCs by changing the concentration of ligands present during synthesis. Adapted from Liu et al.[10] Copyright © 2013 Wiley VCH.

2.3 $Cu_{2-x}Te$ colloidal NCs with LSPR

Following the development of self-doped $Cu_{2-x}S$ and $Cu_{2-x}Se$ NCs with strong LSPR, synthesis of self-doped $Cu_{2-x}Te$ NCs with diverse shapes and strong LSPR was studied. Colloidal $Cu_{2-x}Te$ nanospheres,[15] nanorods,[16] nanocubes[16] and nanoplates[16] (**Fig. 6A**) have been produced by controlling the reaction temperature, reaction time and the concentrations of Cu and Te precursors. An alternative approach to prepare $Cu_{2-x}Te$ NCs involves cation exchange of pre-synthesized CdTe NCs to obtain the $Cu_{2-x}Te$ NCs.[17] The resulting $Cu_{2-x}Te$ NCs maintain the morphology of the templating CdTe NCs, allowing control of the morphology of $Cu_{2-x}Te$ NCs by adjusting the shape of CdTe NCs. Using this methodology, $Cu_{2-x}Te$ NCs with spherical, rod-like and tetrapod-like shapes can be obtained. The shape-dependent plasmonic absorbance in these self-doped $Cu_{2-x}Te$ NCs was studied, demonstrating the presence of different plasmon modes in the $Cu_{2-x}Te$ NCs with anisotropic morphologies.

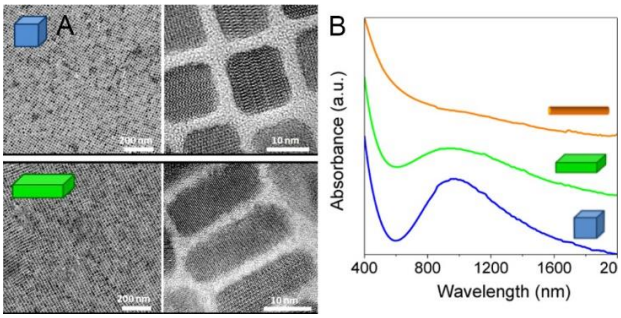

Fig. 6 (A) TEM and HRTEM images of $Cu_{2-x}Te$ nanocubes (top) and nanoplates (bottom), and (B) UV/vis spectra of $Cu_{2-x}Te$ nanorods (orange), nanoplates (green) and nanocubes (blue). Adapted from Li et al.[16] Copyright © 2013 ACS Publications.

2.4 $Cu_{2-x}S_ySe_{1-y}$ alloy NCs with LSPR

Self-doped $Cu_{2-x}S_ySe_{1-y}$ alloy NCs with LSPR have also been synthesized and studied.[11, 18] Simply combining the chalcogenide precursors used for synthesis of $Cu_{2-x}S$ and $Cu_{2-x}Se$ NCs may result in the polydisperse $Cu_{2-x}S_ySe_{1-y}$ NCs, due to differences in reactivity of the S and Se precursors. Balancing the reactivity of the chalcogenide precursors and optimizing the reaction temperature are the key factors in adjusting elemental compositions to tune the LSPR energy, while achieving uniform NC composition, size and shape in the $Cu_{2-x}S_ySe_{1-y}$ NCs. Several combinations including OA-Se/OAm-S, OA-S/OAm-Se, and ODE-S/ODE-Se have been studied.[11, 18] The combination of OA-Se/OAm-S allowed tuning of the S:Se ratio over a relatively wide range.[11] Strong LSPR was observed in these $Cu_{2-x}S_ySe_{1-y}$ NCs due to the presence of copper deficiency. The LSPR frequency blue shifted with increasing elemental fraction of Se in the $Cu_{2-x}S_ySe_{1-y}$ NCs. It also red-shifted with increasing concentration of OA used in synthesis, as discussed further in **section 3.2**.

3. Tuning of the LSPR in self-doped NCs

Manipulating optical properties in nanomaterials is of great interest, and many methods have been developed to tune the LSPR in metal nanostructures. In metals, this is mainly done by varying the nanostructure morphology, as the carrier density in metals is not readily tuned. In contrast, the LSPR in self-doped semiconductor NCs can be tuned by varying the free charge carrier density, which depends not only on the doping level, but also on the NC composition and the nature of the ligands on the NC surface. This allows broad tuning of the LSPR wavelength without dramatic changes in NC size or shape. In this section, we briefly introduce several strategies to manipulate LSPR in self-doped semiconductor NCs, mainly copper chalcogenide NCs.

3.1 Tuning LSPR in $Cu_{2-x}E$ (E=S, Se, Te) NCs by stepwise reaction

The copper deficiency in $Cu_{2-x}E$ (E=S, Se, Te) NCs can be increased by oxidation in air[8, 19] or by intentional stepwise oxidation-reduction reactions using other reagents.[15, 19] Dorfs et al. observed that the copper deficiency was apparently increased in

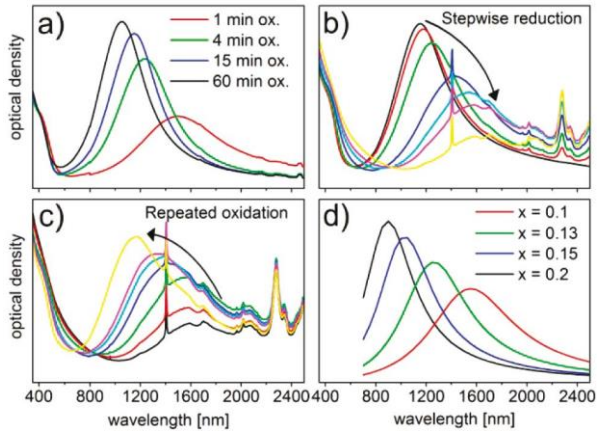

Fig. 7 (a) Time-dependent evolution of the LSPR in $Cu_{2-x}Se$ NCs upon exposure to air. (b) Tuning LSPR through stepwise reduction using $Cu(CH_3CN)_4PF_6$ solution to reduce the cation vacancy concentration in $Cu_{2-x}Se$ NCs. (c) Reversible tuning of LSPR by gradual oxidation in air. (d) Theoretical calculation of extinction spectra of $Cu_{2-x}Se$ NCs with different copper deficiency (x value). Reproduced with permission from Dorfs et al.[19] Copyright © 2011 ACS publications.

$Cu_{2-x}Se$ NCs upon exposing sample to air, and LSPR was dramatically blue-shifted from 1700 nm to 1150 nm (**Fig. 7a**).[19] The $Cu_{2-x}Se$ NCs synthesized by Kriegel et al.[15] exhibited a lower LSPR energy after exposure of the sample to air than that reported by Dorfs et al., although the copper deficiency in these $Cu_{2-x}Se$ NCs was almost the same. This again demonstrates that LSPR in $Cu_{2-x}Se$ NCs depends not only on the cation vacancy concentration, but also on other parameters such as NC size and shape and the nature of ligands on the NC surface. These factors, in turn, depend on the synthesis method. The copper deficiency in $Cu_{2-x}S$ NCs increased only slightly upon oxidization in air, suggesting that air exposure is not equally effective for increasing the carrier concentration in each type of copper chalcogenide NCs.[8] A larger cation vacancy concentration in $Cu_{2-x}Se$ NCs was achieved using solution-phase oxidizing reagents, including a Ce(IV) complex, compared to that achieved using air oxidation.[19]

The reversible reduction of copper deficiency and adjustment of LSPR wavelength in copper chalcogenide NCs can be accomplished by sequential addition of reducing and oxidizing agents. It was first accomplished by adding $Cu(I)(CH_3CN)_4PF_6$ into a $Cu_{2-x}Se$ NC dispersion to reduce the copper deficiency in $Cu_{2-x}Se$ NCs (**Fig. 7b**).[19] The addition of Cu^+ ions was considered to play a key role in reducing the copper deficiency in that work. Kriegel et al. suppressed the LSPR in oxidized copper chalcogenide NCs using diisobutylaluminium hydride (DIBAH), a copper-free reducing agent.[15] They concluded that Cu(II) did not leave the NCs and go into solution upon oxidation. Instead, the Cu(II) may stay on the surface of oxidized copper chalcogenide NCs and can then reinsert into the crystal lattice upon electron injection from a reducing agent. Other reducing reagents, for example $Li(C_2H_5)_3BH$, were also used to tune the LSPR in copper chalcogenide NCs.[14] By combining stepwise oxidation and reduction reactions, one can tune the LSPR in self-doped copper chalcogenide NCs and study the behavior of Cu(II)/Cu(I) and the optical properties during the oxidation-reduction process. However, the limited stability of the NCs after these oxidation or reduction processes may limit the practical applications of the materials.

3.2 *In situ* tuning of LSPR in colloidal NCs by choice of ligand

An alternative means of tuning LSPR in copper chalcogenide NCs is to vary the surface ligands and the elemental composition in alloy NCs, so called *in situ* tuning of LSPR. In colloidal synthesis using OA and OAm-based precursors, the LSPR in $Cu_{2-x}S$ NCs and $Cu_{2-x}Se$ NCs was red-shifted upon increasing the concentration of OA present during the NC synthesis.[10] This was attributed to the deprotonated carboxyl group coordinating to the NC surface, which may act as a hole trap, decreasing the effective density of free holes. The LSPR peaks in $Cu_{2-x}S$ NCs and $Cu_{2-x}Se$ NCs were observed to redshift by 110 nm and 270 nm, respectively using this approach.[10] In $Cu_{2-x}S_ySe_{1-y}$ alloy NCs, the LSPR can shift more significantly than in binary $Cu_{2-x}S$ or $Cu_{2-x}Se$ NCs due to the cooperative effects of elemental composition and surface ligands.[11] The LSPR was observed to blue shift with increasing Se fraction in $Cu_{2-x}S_ySe_{1-y}$ NCs and red shift with increasing concentration of OA used in the synthesis. The blue-shift with increasing Se concentration can be attributed to the lower hole effective mass in $Cu_{2-x}Se$, which is roughly a factor of two smaller than in $Cu_{2-x}S$.[8] As seen in Eq. (1), lower carrier mass produces a higher bulk plasmon frequency and, in turn, shorter LSPR wavelength. These factors simultaneously influence the LSPR energy in the $Cu_{2-x}S_ySe_{1-y}$ alloy NCs and provide the capability of tuning LSPR over a broad spectral range, from 975 nm to 1650 nm, without relying on any post-synthesis chemical reaction (**Fig. 8**).[11] These *in situ* approaches provide colloidally-stable, ligand-capped NCs that are stable in air and therefore relatively easily to use in subsequent applications.

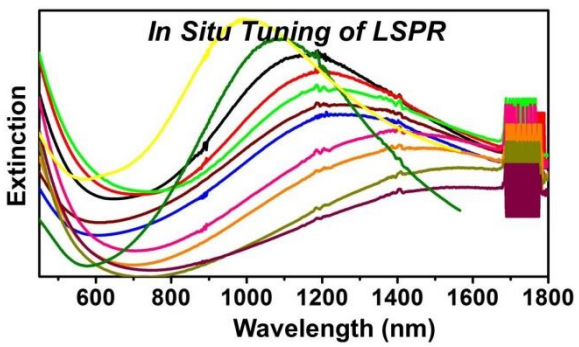

Fig. 8 *In situ* tuning of LSPR in $Cu_{2-x}S_ySe_{1-y}$ ($0< x <1$, $0.4 <y \leq 1$) NCs by controlling the elemental composition and surface ligands. The LSPR wavelength can be tuned from 975 nm to 1650 nm. Reproduced with permission from Liu et al.[11] Copyright © 2013 ACS Publications.

3.3 LSPR in heterogeneous NCs

Multicomponent heterogeneous colloidal NCs can potentially integrate the properties of different classes of materials into a single nanostructure. A prototypical example is the combination of a semiconductor QD with a noble metal NC. Various semiconductor-metal NCs, such as CdSe-Au, with different morphologies and composition have been reported.[20, 21] The optical properties of these semiconductor-metal heterogeneous NCs differ substantially from the sum of their components. For example, the photoluminescence (PL) of the semiconductor QD was quenched by the presence of the metal NC domain.[20] Recently, heterogeneous NCs composed of a heavily-doped semiconductor ($Cu_{2-x}Se$) NC and a metal (Au) NC were synthesized and studied (**Fig. 9A&B**).[22] In contrast to conventional semiconductor NCs or

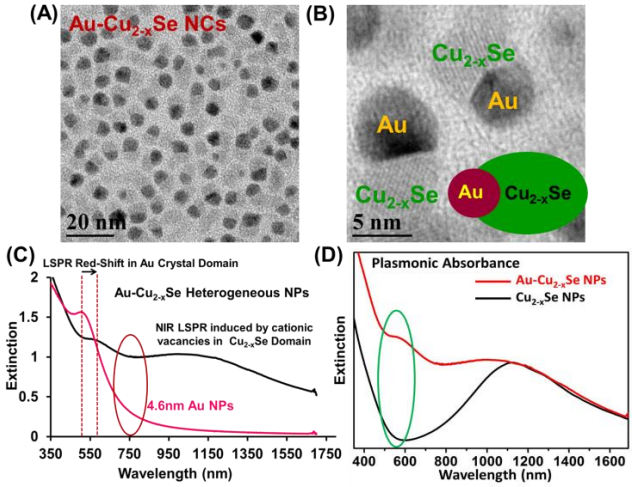

Fig. 9 (A) TEM and (B) HRTEM of Au-$Cu_{2-x}Se$ NCs. (C) LSPR in Au-$Cu_{2-x}Se$ NCs compared with that in Au nanoseeds used for the synthesis. (D) LSPR in Au-$Cu_{2-x}Se$ NCs compared with self-doped $Cu_{2-x}Se$ NCs. Adapted from Liu et al.[22] Copyright © 2013 ACS Publications.

QDs these heavily doped $Cu_{2-x}Se$ NCs do not exhibit appreciable photoluminescence. Instead, as discussed in detail in previous sections, these self-doped $Cu_{2-x}Se$ NCs exhibit LSPR due to the presence of free holes. The Au NC exhibits LSPR at much shorter wavelength, due to its high concentration of free electrons. The direct integration of these two types of plasmonic NCs produces LSPR absorbance over a very broad spectral region from visible to NIR wavelengths. The LSPR in these heterogeneous dimer nanoparticles not only differs from the LSPR of each individual NC (Au and $Cu_{2-x}Se$) but is also not a linear combination of the spectra of the separate NCs (**Fig. 9C&D**).[22] The heterodimer NCs exhibit strong absorbance from 650 to 900 nm where the parent NCs both have much weaker absorbance. The LSPR absorbance may be influenced by charge carrier redistribution in the heterogeneous Au-$Cu_{2-x}Se$ NCs, with free holes diffusing from $Cu_{2-x}Se$ to Au and electrons delocalized from Au to $Cu_{2-x}Se$. These two effects reduce the free carrier concentration in both domains. Each of the resonances is also influenced by the frequency-dependent dielectric properties of the adjacent domain. Further studies will be required to provide full understanding of the optical properties of these heterogeneous NCs. Nonetheless, this approach offers a new strategy for engineering LSPR in small colloidal NCs by coupling two different types of plasmonic NCs without relying on much larger hollow or anisotropic structures (e.g. gold nanoshells, nanorods, and nanocages) to achieve NIR absorbance. The small size of these structures facilitates their use for *in vivo* applications. Their broad absorbance, spanning the visible and NIR spectral ranges, allows flexibility in choice of wavelengths for imaging and phototherapy applications.

4. Extrinsically-doped colloidal NCs with LSPR

4.1. Colloidal indium tin oxide (ITO) NCs

Tin (Sn)-doped indium oxide (In_2O_3) is a prototypical transparent conductive oxide (TCO) material, which consists of a metal oxide semiconductor, In_2O_3, doped with a group IV element, Sn. The crystalline In_2O_3 host matrix has a large band gap, and is therefore optically transparent. The Sn dopants provide free charge carriers that are largely responsible for the conductivity. Thin films

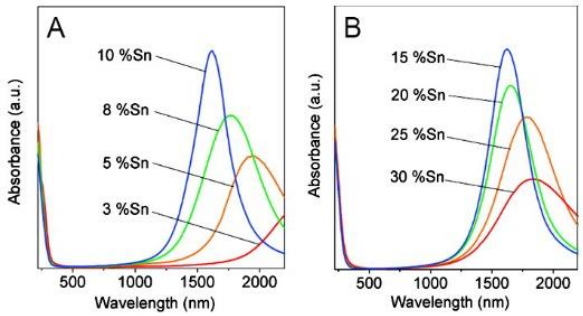

Fig. 10 Extinction spectra showing (A) the decrease of LSPR wavelength with increasing dopant concentration (% Sn) up to 10% Sn, and (B) increase of LSPR wavelength with increasing dopant concentration beyond 15% Sn. Adapted from Kaneharn et al.[23] Copyright © 2009 ACS Publications.

of ITO and related transparent conductive oxides are widely used in photovoltaics, touch screens, LCD displays, and many other applications. Based on the high concentration of free charge carriers in ITO, ITO NCs can be expected to exhibit LSPR. Formation of high-quality colloidal ITO NCs with tunable composition using solution-phase chemical synthesis was demonstrated by Kanehara et al.[23] The LSPR in these colloidal ITO NCs could be tuned from 1618 nm to >2200 nm by controlling the Sn concentration (**Fig. 10**). The colloidal dispersibility of ITO NCs provides promise for fabricating transparent conductive films/electrodes based on solution-phase processing technologies including coating, printing, spraying and blading. Moreover, dynamic modulation of surface plasmon resonance in ITO NC thin films using electrochemical control has been reported.[24] The charge carrier density in ITO NCs can be manipulated by applying a bias voltage, which in turn influences the frequency of the surface plasmon resonance. These methods of manipulating plasmonic absorbance in ITO NCs provide the possibility of using the ITO NCs for electrochromic[24] and optoelectronic applications, as discussed in **sections 5.3** and **5.4**.

4.2. ZnO NCs doped with group III elements

Similar to ITO NCs, ZnO NCs doped with group III elements have considerable density of free charge carriers. Relative to ITO, doped ZnO has the advantage of being based upon relatively low-cost, earth abundant elements. This could be important for long-term viability in photovoltaics, displays, etc. High-quality n-type colloidal ZnO NCs have been produced by chemical solution methods. Buonsanti et al. reported colloidal aluminium (Al)-doped ZnO (AZO) NCs with controlled doping level and NC size.[25] The dopant concentration and average size were tuned from 1.4% to 7.3% and from 5 to 20 nm, respectively, by varying the temperature for nucleation and NC growth as well as the Al precursor concentration. The AZO NCs synthesized by this method exhibit LSPR at NIR wavelengths, which is enhanced with increased dopant concentration. Della Gaspera et al. developed a method for synthesis of colloidal gallium (Ga)-doped ZnO (GZO) NCs.[26] The incorporation of Ga^{3+} ions into ZnO NCs resulted in NIR LSPR, which was attributed to the presence of free electrons from hypervalent doping. Moreover, a small increase in LSPR was observed in Ga-doped ZnO NCs treated with hydrogen although the mechanism of this change was not entirely clear.

4.3. LSPR in other metal oxide and doped metal oxide NCs

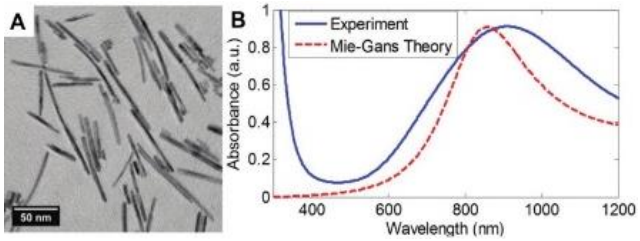

Fig. 11 (A) TEM images of $WO_{2.83}$ nanorods. (B) Experimental measurement and theoretical simulation of LSPR in $WO_{2.83}$ nanorods. Adapted from Manthiram et al.[27] Copyright © 2012 ACS Publications.

Beyond ITO and AZO NCs, which are the dominant TCO materials used in industry, some other metal oxide and doped metal oxide NCs have also exhibited LSPR. Tungsten oxide ($WO_{3-\delta}$) is an electrochromic material with potential applications in fabrication of smart windows. The free carriers responsible for the electrochemically-tunable optical absorbance arise from the presence of oxygen vacancies in non-stoichiometric $WO_{3-\delta}$. This effect is somewhat similar to self-doped copper chalcogenide NCs. Colloidal $WO_{3-\delta}$ nanorods (**Fig. 11A**) were synthesized by decomposition of tungsten(V) ethoxide in the presence of OA and trioctylamine (TOA).[27] The resulting NCs had a $WO_{2.83}$ composition and a well-defined rod-like morphology. The $WO_{2.83}$ nanorods exhibit a strong LSPR with a peak centered near 900 nm (**Fig. 11B**), arising from the outer-d valence electrons in the transition metal oxide. The LSPR spectrum was modelled using Mie-Gans theory which was in remarkably consistent with the experimental observation.[27] In addition, heating the $WO_{2.83}$ nanorods in air induced a red shift of the LSPR due to a decrease in the density of oxygen vacancies. This provides a simple method of tuning the LSPR in oxygen-deficient metal oxide NCs. Rhenium (Re) has only one more outer-d valence electron than W. The optical properties of rhenium oxide (ReO_3) NCs were studied by Biswas and Rao.[28] The colloidal ReO_3 NCs exhibited LSPR in the visible spectral region from 488 to 534 nm. The very high energy LSPR, comparable to that of gold, reflects the metallic behavior of ReO_3.

Colloidal oxygen-deficient molybdenum trioxide (MO_{3-x}) NCs provide another example of plasmonic transition metal oxide nanomaterials.[29] MO_{3-x} nanosheets with ~3.3 nm thickness were synthesized by hydrothermal decomposition of ammonium molybdate in an oil/water emulsion. The nanosheets display LSPR ranging from 600 nm to 1200 nm. Upon oxidation, MO_{3-x} nanosheets with a blue color evolved to nanosheets that were white in color. The original LSPR in MO_{3-x} nanosheets was gradually depressed with increasing oxidization time and diminished after 24 hours. This was attributed to conversion of Mo^{V} to Mo^{VI}.

Titanium dioxide (TiO_2) is a semiconductor with a wide band gap that is widely used in paper, cosmetics and coatings as well as more recent applications such as photocatalysis and dye-sensitized solar cells. Gordon et al. reported a post-synthetic protocol to produce TiO_2 nanostructures with tailorable morphology by seed growth.[30] The TiO_2 nanostructures synthesized using TiF_4 as the precursor showed a blue color rather than the typical white color of TiO_2. This blue color, also observed in titania produced by high-temperature flame-based processes, is associated with oxygen deficiency and the presence of Ti^{3+} ions in the TiO_2 lattice.[31] Gordon et al. observed LSPR at mid-IR wavelengths in TiO_2 NCs synthesized using TiF_4 but not in that prepared from $TiCl_4$.[30] The LSPR was attributed to oxygen vacancies induced by fluorine doping as well as the presence of Ti^{3+}, demonstrated by electron

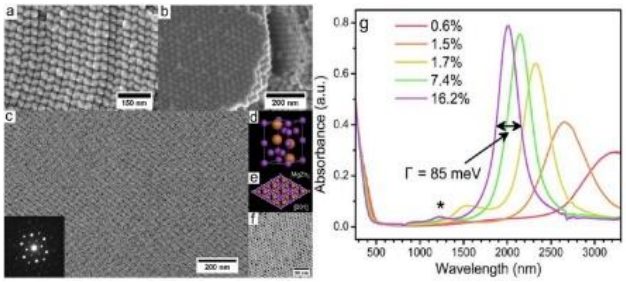

Fig. 12 (A) and (B) SEM images of self-assembled ICO octahedral NCs forming a superlattice. (C) Long range [001] projection of the $MgZn_2$-type binary NC superlattice. (D) and (E) unit cell and [001] projection of the $MgZn_2$-type binary NC superlattice. (F) TEM images of ICO superlattice. (G) Evolution of LSPR in colloidal ICO NCs with increasing dopant concentration. Adapted with permission from Gordon et al.[33] Copyright © 2013 ACS Publications.

paramagnetic resonance (EPR) and X-ray photoelectron spectroscopy (XPS). The presence of oxygen vacancies was also experimentally confirmed by annealing the samples at 300 ºC in air, which decreased the oxygen vacancy concentration and converted the blue TiO_2 to ordinary white TiO_2. In addition to the LSPR observed in oxygen-deficient TiO_2 nanostructures, extrinsic doping of TiO_2 nanostructures can provide an appreciable density of free charge carriers, sufficient to generate LSPR. Niobium (Nb)-doped TiO_2 NCs were synthesized and studied by Trizio et al.[32] A broad LSPR from the visible to mid-IR wavelengths was observed, which increased in intensity with increasing concentration of dopants (Nb^{5+}). The substitution of Ti^{4+} by Nb^{5+} provides free electrons in the conduction band that lead to the observed LSPR.

Other extrinsically doped metal oxide NCs include cadmium oxide (CdO) doped with indium. Indium cadmium oxide (ICO) NCs with well-defined size and controlled morphology, including rods, plates, and octahedra, were obtained by organic solution-phase synthesis.[33] The free conduction electrons in ICO NCs, which result from the heavy doping, lead to LSPR (**Fig. 12**). The high extinction coefficient in the range from 10^8 $M^{-1}cm^{-1}$ to 10^9 $M^{-1}cm^{-1}$ (calculated at λ_{max}) shows that the absorbance cross-sections of these ICO NCs are comparable to that of metal NPs of similar size. Three-dimensional (3-D) superlattice ICO films were formed by self-assembly of ICO NCs from their colloidal dispersion (**Fig. 12**). This provides a potential path to metamaterials fabricated by self-assembly of colloidal NC building blocks.[33]

4.4. LSPR in doped Silicon NCs

Silicon (Si) is the primary material used in the current microelectronics industry. The abundance of Si and its current role in integrated circuits and photovoltaics help to make nanostructured Si a promising material for next-generation nanoelectronics and nano-optoelectronics. Developing methods for synthesizing and modifying the surface of Si nanostructures, studying their physical and chemical properties, and exploring their potential applications have attracted substantial attention over the past two decades. In microelectronics applications of silicon, group III and V elements are generally used to achieve p- and n-type doping. Phosphorous (P) is the prototypical n-type dopant for silicon. The presence of free charges in heavily-doped Si provides the possibility of generation of LSPR.

P-doped Si NCs have been synthesized by radio-frequency (RF)

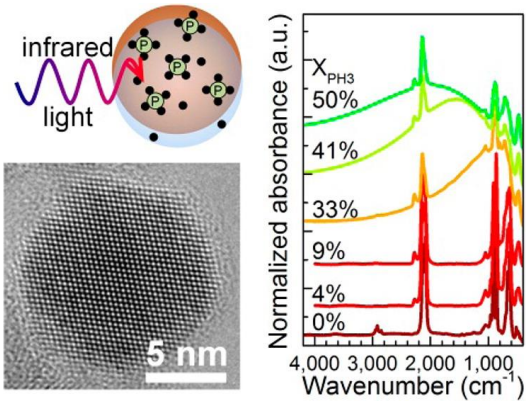

Fig. 13 (A) Schematic of LSPR of P-doped Si NCs. (B) HRTEM of a single P-doped Si NC. (C) FTIR spectrum of P-doped Si NCs. The broad absorbance band corresponds to the LSPR in P-doped Si NCs. Reproduced with permission from Rowe et al.[34] Copyright © 2013

nonthermal plasma pyrolysis of silane (SiH_4) diluted in hydrogen, with a small amount of phosphine (PH_3) as the dopant precursor.[34] Fourier transform infrared spectroscopy (FTIR) revealed a broad absorbance with sharp peaks, corresponding to vibrational modes of surface species, superimposed on it (**Fig. 13C**). The broad absorbance resulted from the free charge carriers contributed by the P dopants, which produce a LSPR. The absence of the broad absorbance in undoped Si NCs supports the interpretation of the absorbance as arising from a LSPR.[34] Moreover, the absorbance blue-shifted with increasing dopant concentration, due to the dependence of LSPR on the concentration of free charge carriers, as discussed above. Note that the dopant concentrations in **Fig. 13** are much higher than those typically used in microelectronics. A blue shift of the LSPR was also achieved by annealing the doped Si NCs. This was attributed to passivation of the surface, freeing charge carriers from surface traps associated with surface "dangling bonds" or other defects. Surface doping of Si NCs through hypervalent interaction between the Si NC surface and donor molecules was subsequently reported by the same group.[35] In this case, the Si NCs were synthesized by pyrolysis of silicon tetrachloride ($SiCl_4$) gas in a nonthermal plasma reactor. The resulting chlorine (Cl)-terminated Si NCs can be dispersed in ketones, aldehydes and nitriles which have ─C=O or ─C≡N groups that stabilize the Si NC surface by hypervalent interaction and, simultaneously, act as electron donors. The nominally undoped silicon NCs passivated by these molecules exhibit LSPR, the intensity of which decreases upon evaporation of the solvent molecules. This suggests that the doping is associated with these organic molecules, which can provide electrons to the Si NC surface.[35]

4.5. Summary of Plasmonic Semiconductor and Metal Oxide NCs

Table 1 summarizes the varieties of heavily-doped semiconductor and metal oxide NCs with LSPR.

Table 1. Summary of reported semiconductor and metal oxide plasmonic NCs

Materials (Nanocrystals)	LSPR peak wavelength (nm)	References
$Cu_{2-x}S$	975 ─ 1800	7,8,9,10,15
$Cu_{2-x}Se$	970 ─ 1800 1700	10,13,14,15,19,45
$Cu_{2-x}Te$	900 ─ 1103	15,16,17
$Cu_{2-x}S_ySe_{1-y}$	975 ─ 1650	11, 18
Au-$Cu_{2-x}Se$	broad LSPR	22
ITO	1618 ─ >2200	23,24
Al-doped ZnO	>2500	25
Ga-doped ZnO	>2500	26
$WO_{3-\delta}$	~ 900	27
ReO_3	488 ─ 534	28
MO_{3-x}	~ 900	29
TiO_2	~ 3400	30
Nb-doped TiO_2	>2500	32
ICO	1800 ─ 3500	33
P-doped Si	>2500	34
GeTe	~2500	36

5. Applications of NCs with LSPR

5.1. Bioimaging

Nanoparticle-based bioimaging has attracted considerable attention over the past fifteen years.[2, 37] Plasmonic nanostructures[2, 38] and photoluminescent QDs[37] have been used as contrast agents and fluorescent biomarkers for many *in vivo* and *in vitro* imaging modalities including fluorescence imaging,[37] photoacoustic imaging,[39] photothermal imaging,[38] dark field imaging,[40] etc. Plasmonic nanomaterials used for biomedical applications should ideally exhibit LSPR in the NIR spectral region where tissue and biomolecules exhibit relatively weak scattering and absorbance, allowing deep penetration of light *in vivo*.[41] Conventional colloidal Au NPs with spherical shape and diameter of 20 nm or less generally have LSPR near 530 nm. To achieve NIR absorbance, anisotropic or hollow Au nanostructures have been developed and synthesized by numerous methods[2, 6] involving growth of Au nanorods based on Au nanoseeds, creation of Au nanocages by titrating silver nanocubes with auric chloride, growth of Au nanoshells on silica microsphere templates, etc. These Au nanostructures with NIR plasmonic absorbance have been widely studied as contrast agents for bioimaging. Progress in developing plasmonic heavily-doped NCs over the past few years provides an alternative to Au nanostructures. Due to their lower density of free charge carriers, these colloidal doped semiconductor NCs can directly exhibit LSPR in the NIR spectral region despite their small size (≤10 nm). Doped NCs with NIR LSPR that does not rely on finely manipulating shape and size open up new possibilities for applications in plasmonic nanomaterials-based bioimaging.[22, 42, 43] However, not all of the doped NPs with NIR LSPR can be used for these applications because the absorbance of water increases sharply at wavelengths above 1200 nm. Many of the extrinsically-doped NPs such as ITO and AZO have plasmonic absorbance with a peak wavelength longer than 1350 nm, where light absorbance by water severely limits the imaging depth.

Photoacoustic (PA) imaging, which includes photoacoustic tomography (PAT), is an emerging non-invasive and non-ionizing imaging modality that integrates the optical and ultrasound imaging methodologies to achieve high resolution at relatively deep tissue depth.[41] In PA imaging, a laser pulse induces rapid heating of a structure to be imaged, and this heating generates a pressure wave, i.e., an acoustic signal. The acoustic signal is detected by a conventional ultrasound imaging system. PA imaging can be implemented by taking the advantage of intrinsic

optical contrast in biological systems, for example contrast arising from haemoglobin and melanin, which can absorb light and generate an acoustic signal.[41] This makes PA imaging effective for imaging structures such as blood vessels without using any extrinsic contrast agents. These intrinsic contrast mechanisms generally produce absorbance in the visible spectral region that may limit the imaging depth. To facilitate deep tissue imaging, a strong, extrinsic NIR light absorber is desirable for use as a contrast agent.[41] Such substances are also called exogenous contrast agents. Au nanostructures with NIR LSPR have shown significant promise as exogenous contrast agents for PA imaging. More recently, self-doped copper chalcogenide NCs with NIR LSPR have also emerged as promising exogenous contrast agents.

Ku et al. studied the use of self-doped $Cu_{2-x}S$ NPs as a contrast agent for brain and lymph node (LN) PA imaging.[42] Because the lymphatic system is a pathway for cancer metastasis, lymph node mapping is important for diagnosing the metastatic stage of cancer. $Cu_{2-x}S$ NPs of 11 nm mean diameter were synthesized by reacting $CuCl_2$ with Na_2S in water at 90 ºC. The $Cu_{2-x}S$ NPs had a broad NIR absorbance with a peak centered near 990 nm. This allows the use of the cost-effective Nd:YAG laser source (with a wavelength of 1064 nm) to excite the NPs. $Cu_{2-x}S$ NPs functionalized with polyethylene glycol (PEG) were used as the contrast agent for PA imaging. They diffused into the cerebral cortex and LNs of the rats following intracranial injection and interstitial injection into the front paw pad, respectively. The brain and LNs were monitored by PA imaging after NP injection. A LN 12 mm below the skin surface could be clearly visualized using $Cu_{2-x}S$ NPs as the contrast agent, excited by a Nd:YAG laser source with a power of 100 mJ/cm^2, which is considered the maximum permissible exposure intensity for human skin at 1064 nm wavelength.

$Cu_{2-x}Se$ NPs were also studied as a contrast agent for PA imaging.[43] $Cu_{2-x}Se$ NPs with a 7.6 nm mean size were synthesized in organic solvent. Then, aqueous $Cu_{2-x}Se$ NP micelles were formed by encapsulating $Cu_{2-x}Se$ NPs in polyethyleneglycol-grafted phospholipid (DSPE-PEG) through self-assembly. 180 min after injection of $Cu_{2-x}Se$ NP micelles into the left forearm of a rat, the accumulation of $Cu_{2-x}Se$ NP micelles in the sentinel lymph nodes (SLNs) provided clear visualization of SLNs by photoacoustic imaging.[43] These results demonstrate that self-doped copper chalcogenide NPs are a promising alternative to anisotropic or hollow Au nanostructures as NIR contrast agents for PA imaging.

As discussed in **section 3.3** above, Au-$Cu_{2-x}Se$ heterogeneous NPs with ~10 nm overall size have a broad absorbance spanning the visible and NIR spectral regions, offering the opportunity to use a cost-effective 1064 nm laser source for excitation, while also permitting use of existing instrumentation with laser sources at other NIR wavelengths. Their broad absorbance also enables multi-modal imaging using both PAT and dark-field optical imaging. Their absorbance in the range of 700-900 nm within the biological window of transparency is higher than that of the pure $Cu_{2-x}Se$ NCs. To investigate the Au-$Cu_{2-x}Se$ NPs for PA imaging, thiol-PEG was used to functionalize the Au-$Cu_{2-x}Se$ NPs and make them dispersible in water and biological media. The PEGylated Au-$Cu_{2-x}Se$ NPs prepared by ligand-exchange resisted aggregation and maintained their small size after dispersion in water. The time-dependent *in vivo* PA imaging of SLN was studied by monitoring

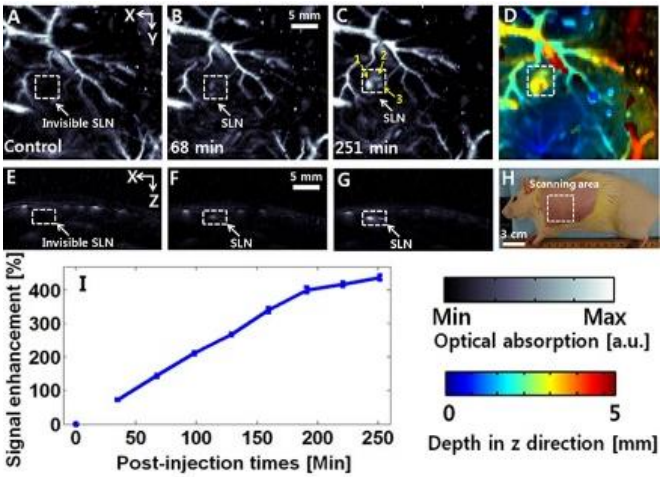

Fig. 14 *In vivo* SLN photoacoustic images. PA images were acquired before (A) and after the injection of Au-$Cu_{2-x}Se$ NPs: (B) 68 min and (C) 251 min after injection. Three lymph nodes indicated with 1−3 are visible in the axillary region. (D) Depth-encoded PA coronal MAP image of (C). (E−G) Depth-resolved cross-sectional B-scan images of A−C, respectively. (H) Photograph of an animal with hair removed before PA imaging. (I) Time-dependent accumulation of Au-$Cu_{2-x}Se$ NPs in a SLN, in terms of the amplitude changes of PA signal. Copyright © 2013 ACS Publishing Group, reproduced with permission from Liu et al.[22]

the SLNs after injecting Au-$Cu_{2-x}Se$ NPs (**Fig. 14**). The SLN could be clearly visualized after accumulation of Au-$Cu_{2-x}Se$ NPs. Moreover, other draining LNs were delineated, indicating that the small Au-$Cu_{2-x}Se$ NPs can diffuse through the lymphatic system. The *in vivo* imaging depth using Au-$Cu_{2-x}Se$ NPs as contrast agents reached 17 mm. Because the depth of SLNs in human breasts is about 12 ± 5 mm below the skin surface and the laser power used here was only 1/10 of the ANSI safety limit, the Au-$Cu_{2-x}Se$ NPs with small particle size have significant clinical relevance from the prospective of imaging depth achieved, low intensity of laser power required and the expected biocompatibility of the materials.

5.2. Photothermal Therapy

The photothermal effect refers to heat generated by absorption of light. In photothermal therapy, exogenous agents including plasmonic nanomaterials and organic dyes are introduced into a biological system for light absorption and heat generation. Here, we focus the use of plasmonic nanomaterials for photothermal therapy. Photothermal therapy refers to the use of optical heating of a targeted structure, e.g. a tumor, to kill diseased cells. Photothermal therapy employing metal nanostructures has reached clinical trials.[44] Similar to NP-based bioimaging, the anisotropic and hollow Au nanostructures with NIR plasmonic absorbance including nanoshells, nanocages, nanorods and nanostars have been proposed and studied as agents for photothermal therapy.[2] Recently, use of the NIR LSPR in doped semiconductor NPs for photothermal therapy has attracted increased interest, again because it could allow strong NIR absorbance by very small nanoparticles with favourable *in vivo* circulation, biodistribution, and excretion profiles.[45, 46]

Hessel et al. investigated the use of $Cu_{2-x}Se$ NPs for cancer cell photothermal therapy and compared their effectiveness to that of Au nanostructures with NIR plasmonic absorbance.[45] $Cu_{2-x}Se$ NPs with ~16 nm mean size and NIR LSPR centered at 970 nm were synthesized in organic solvent using CuCl and selenourea as the

Cu and Se precursors, respectively. The colloidal $Cu_{2-x}Se$ NPs were functionalized by an amphiphilic polymer to provide aqueous dispersibility for studying the photothermal effect. The photo-induced heat generated in $Cu_{2-x}Se$ NPs was compared with that of Au nanorods and Au nanoshells after normalizing by the extinction of each dispersion. This study showed that photo-induced heat generated by $Cu_{2-x}Se$ NPs is comparable to that from Au nanorods and higher than that from Au nanoshells. Moreover, measurements of photothermal transduction efficiency, an important metric for photothermal therapy, indicated that the $Cu_{2-x}Se$ NPs photothermal efficiency (22%) was equal to or slightly greater than that of commercially-available Au nanorods (21%), and much higher than that of commercially available Au nanoshells (13%). The high photothermal transduction efficiency results from the fact that the small $Cu_{2-x}Se$ NPs have relatively low scattering contribution to optical extinction, and corresponding high absorption contribution. Scattered light does not contribute to the photothermal effect. In addition, the small size of the $Cu_{2-x}Se$ NPs may improve the *in vivo* blood circulation time. The ablation of HCT-116 cells was demonstrated using an 800 nm laser to irradiate the cells after uptake of the $Cu_{2-x}Se$ NPs.

The photothermal effect of copper chalcogenide NPs may be enhanced, relative to gold nanostructures, if a longer wavelength laser source is used for excitation. The plasmonic absorbance of most colloidal Au nanostructures tested for photothermal therapy to date decreases strongly at wavelengths beyond 950 nm. As shown in section 2, self-doped copper chalcogenide NPs can have an LSPR peak at longer wavelengths, e.g. from 975 to 1650 nm for $Cu_{2-x}S_ySe_{1-y}$ (**Fig. 8**). A recent report showed a slightly higher value of photothermal conversion efficiency (25.7%) in Cu_9S_5 NPs than in Au nanorods (23.7% in that study), using a 980 nm laser for excitation.[46] Although the photothermal conversion efficiency of Au nanostructures tested in these studies was lower than that reported in some other papers, those differences may simply reflect the different measurement conditions. Accepted standard methods for measuring photothermal transduction efficiency are not yet well established. In any case, these studies clearly demonstrate that the self-doped copper chalcogenide NPs have strong photothermal conversion efficiency and merit further investigation as agents for photothermal therapy.

In vivo photothermal therapy was executed by irradiating a tumor injected with the Cu_9S_5 NPs using a 980 nm laser at an intensity of 0.51 W/cm^2.[46] Histopathology revealed that cancer cells were photothermally ablated. Moreover, use of copper telluride NPs for *in vitro* photothermal therapy was also reported.[16] These investigations all demonstrate that self-doped copper chalcogenide NPs are viable alternatives to metal nanostructures for use in photothermal therapy.

5.3. Electrochromic Materials for "Smart Windows" and related applications

Electrochromic materials are the class of materials whose optical properties can be reversibly tuned by an applied voltage. Transition metal oxides are very promising materials for electrochromic devices because they can form non-stoichiometric phases and exhibit electrochromism due to the intervalence charge-transfer optical transitions.[47] Electrically-tunable LSPR can play a role in such materials.

Engineering NIR plasmonic absorbance in doped metal oxide

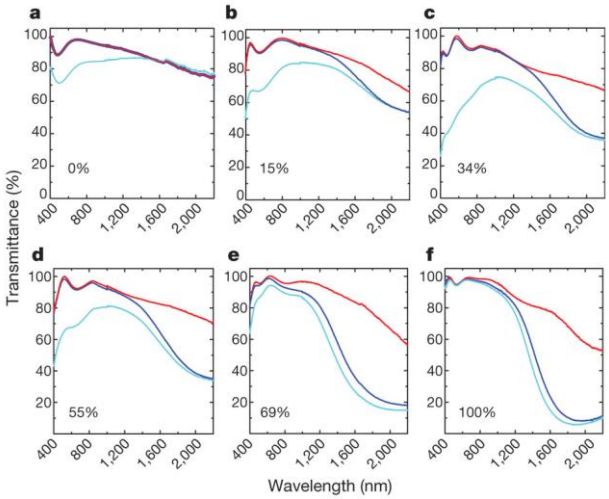

Fig. 15 (a)-(f) Transmittance spectra of ITO-in-NbO_x with different ITO nanocrystal content under an applied electrochemical voltage (4V in red, 2.3V in blue and 1.5V in cyan, versus Li/Li$^+$). Adapted from Llordés et al.[48] Copyright © 2013 Nature Publishing Group.

NCs through electrochemical control has been reported.[24] By manipulating the free charge carrier density in ITO NCs, the NIR LSPR was dynamically and reversibly modulated, shifting by up to 1200 nm without relying on ion intercalation. This demonstrates the promise of plasmonic nanomaterials in the field of electrochromism. Progress in NC-based electrochromism has shown that electrochromic optical switching behaviour can be manipulated over a wide spectral range from the visible to NIR spectral region by coupling plasmonic ITO NCs with amorphous niobium oxide glass (NbO_x).[48] ITO NCs encapsulated by polyniobate clusters (POMs) were formed chemically, then converted to nanocomposites of ITO NC in NbO_x glass upon annealing. The NbO_x glass with integrated ITO NCs shows considerable enhancement in optical contrast at visible wavelengths, compared to pure NbO_x glass. The tunability of LSPR in ITO NCs through electrochemical control dramatically extends the electrochromic spectrum from the visible to the NIR spectral region (**Fig. 15**). NIR electrochromism is of particular interest for controlling heat transmission through "smart windows" independently of visible light transmission, for example blocking NIR wavelengths in the summer, and transmitting them in the winter. The electrochromic functionality in the ITO- NbO_x glass composites can be tuned by controlling the content of ITO NCs in the composites and the bias voltage applied. This work presents a prototype and again illustrates the potential of plasmonic nanomaterials in electrochromic applications such as smart windows.[48]

5.4. Solution-Processed Transparent Conductive Films

Doped metal oxides such as ITO and AZO are widely used to fabricate transparent electrodes in industry. The current fabrication techniques used in industry involve deposition from the vapour phase that generally requires high energy input and large capital investment in high vacuum processing equipment. Colloidal dispersions of NCs provide the possibility of fabricating TCO films or electrodes by low-temperature atmospheric-pressure solution-phase processing technologies. Many studies have demonstrated production of high-quality colloidal ITO NCs by chemical solution methods.[23, 49] The ITO thin films fabricated from

these NC dispersions exhibit high transmittance at visible wavelengths. Relatively high conductivity was observed in these ITO NC thin films due to the presence of the free charge carriers contributed by the dopants. This is consistent with the observation of LSPR in colloidal ITO NC dispersions, arising from the considerable density of free charge carriers. Herein, LSPR is actually another manifestation of the presence of the free charge carriers, but is not directly related to the application. However, the thin films assembled from ITO NC dispersions still shows lower conductivity than those made by conventional methods such as sputtering.[49] This can be attributed to the formation of defects in the film during the coating process as well as the small grain size of NC inducing charge carrier scattering. Similar investigations were also made for colloidal AZO[25] and GZO[26] NCs. The results show the potential of fabricating TCO thin films by solution-phase processing based on colloidal NCs, but further progress is needed for these films to match the performance of vacuum-deposited films.

An exciting new area of application of thin films and nanostructures of plasmonic semiconductors is in optical metamaterials. Several studies have shown that heavily-doped semiconductors can have important advantages over noble metals in these applications, as discussed in detail by Naik et al.[50] and many references cited therein. To date, the plasmonic semiconductors used in metamaterial applications have been deposited and patterned by vacuum deposition methods and photolithography. However, here, as in other TCO applications, colloidal plasmonic semiconductors may eventually enable low-cost solution phase processing and patterning.

6. Conclusion and Outlook

The study of heavily-doped semiconductor and metal oxide nanoparticles that exhibit LSPR is a relatively young and rapidly-advancing research field. This group of novel plasmonic nanomaterials provides a potential alternative to metal nanostructures in several applications, and opens up new applications where absorbance at NIR and mid-IR wavelengths is needed. Much research in this field to date has involved developing methods for synthesizing high-quality colloidal NCs, exploring new types of nanomaterials with LSPR, and fundamentally studying the optical properties of these nanomaterials. These materials have begun to be explored for varied applications, including theranostics, optoelectronics, and sensing. This tutorial review aims to summarize key aspects of this research field, comparing and contrasting the variety of materials and potential applications that are currently being considered. We hope this will help to guide researchers entering this research area. A great amount of work is still needed to develop practical applications of these novel types of plasmonic nanomaterials. For example, comprehensive analysis of cytotoxicity, biodistribution, and biodegradability of these materials, based on systematic investigations, will be required in order to move forward with their biomedical applications. The potential advantages of these materials such as small size also need to be further assessed, and the materials must be optimized to best exploit these advantages.

Notes and references

[a] *Department of Chemical and Biological Engineering, University at Buffalo (SUNY), 310 Furnas Hall, Buffalo, New York, 14260-4200 USA. Fax: +1(716)645-3822; Tel: +1(716)645-1181; E-mail: swihart@buffalo.edu*

1. S. A. Maier, *Plasmonics: Fundamentals and Applications*, Springer, 2007.
2. E. C. Dreaden, A. M. Alkilany, X. H. Huang, C. J. Murphy and M. A. El-Sayed, *Chem. Soc. Rev.*, 2012, **41**, 2740-2779.
3. E. Ozbay, *Science*, 2006, **311**, 189-193.
4. M. Faraday, *Philos. Trans. R. Soc. London*, 1857, **147**, 145-181.
5. H. J. Chen, L. Shao, Q. Li and J. F. Wang, *Chem. Soc. Rev.*, 2013, **42**, 2679-2724.
6. M. Grzelczak, J. Perez-Juste, P. Mulvaney and L. M. Liz-Marzan, *Chem. Soc. Rev.*, 2008, **37**, 1783-1791.
7. Y. X. Zhao, H. C. Pan, Y. B. Lou, X. F. Qiu, J. J. Zhu and C. Burda, *J. Am. Chem. Soc.*, 2009, **131**, 4253-4261.
8. J. M. Luther, P. K. Jain, T. Ewers and A. P. Alivisatos, *Nat. Mater.*, 2011, **10**, 361-366.
9. S. W. Hsu, K. On and A. R. Tao, *J. Am. Chem. Soc.*, 2011, **133**, 19072-19075.
10. X. Liu, X. L. Wang, B. Zhou, W. C. Law, A. N. Cartwright and M. T. Swihart, *Adv. Funct. Mater.*, 2013, **23**, 1256-1264.
11. X. Liu, X. L. Wang and M. T. Swihart, *Chem. Mater.*, 2013, **25**, 4402-4408.
12. S. C. Riha, D. C. Johnson and A. L. Prieto, *J. Am. Chem. Soc.*, 2011, **133**, 1383-1390.
13. S. Deka, A. Genovese, Y. Zhang, K. Miszta, G. Bertoni, R. Krahne, C. Giannini and L. Manna, *J. Am. Chem. Soc.*, 2010, **132**, 8912-8914.
14. W. H. Li, R. Zamani, M. Ibanez, D. Cadavid, A. Shavel, J. R. Morante, J. Arbiol and A. Cabot, *J. Am. Chem. Soc.*, 2013, **135**, 4664-4667.
15. I. Kriegel, C. Y. Jiang, J. Rodriguez-Fernandez, R. D. Schaller, D. V. Talapin, E. da Como and J. Feldmann, *J. Am. Chem. Soc.*, 2012, **134**, 1583-1590.
16. W. H. Li, R. Zamani, P. R. Gil, B. Pelaz, M. Ibanez, D. Cadavid, A. Shavel, R. A. Alvarez-Puebla, W. J. Parak, J. Arbiol and A. Cabot, *J. Am. Chem. Soc.*, 2013, **135**, 7098-7101.
17. I. Kriegel, J. Rodriguez-Fernandez, A. Wisnet, H. Zhang, C. Waurisch, A. Eychmuller, A. Dubavik, A. O. Govorov and J. Feldmann, *ACS Nano*, 2013, **7**, 4367-4377.
18. E. Dilena, D. Dorfs, C. George, K. Miszta, M. Povia, A. Genovese, A. Casu, M. Prato and L. Manna, *J. Mater. Chem.*, 2012, **22**, 13023-13031.
19. D. Dorfs, T. Hartling, K. Miszta, N. C. Bigall, M. R. Kim, A. Genovese, A. Falqui, M. Povia and L. Manna, *J. Am. Chem. Soc.*, 2011, **133**, 11175-11180.
20. T. Mokari, E. Rothenberg, I. Popov, R. Costi and U. Banin, *Science*, 2004, **304**, 1787-1790.
21. W. L. Shi, H. Zeng, Y. Sahoo, T. Y. Ohulchanskyy, Y. Ding, Z. L. Wang, M. Swihart and P. N. Prasad, *Nano Lett.*, 2006, **6**, 875-881.
22. X. Liu, C. Lee, W.-C. Law, D. Zhu, M. Liu, M. Jeon, J. Kim, P. N. Prasad, C. Kim and M. T. Swihart, *Nano Lett.*, 2013, **13**, 4333-4339.
23. M. Kanehara, H. Koike, T. Yoshinaga and T. Teranishi, *J. Am. Chem. Soc.*, 2009, **131**, 17736-17737.

24. G. Garcia, R. Buonsanti, E. L. Runnerstrom, R. J. Mendelsberg, A. Llordes, A. Anders, T. J. Richardson and D. J. Milliron, *Nano Lett.*, 2011, **11**, 4415-4420.
25. R. Buonsanti, A. Llordes, S. Aloni, B. A. Helms and D. J. Milliron, *Nano Lett.*, 2011, **11**, 4706-4710.
26. E. Della Gaspera, M. Bersani, M. Cittadini, M. Guglielmi, D. Pagani, R. Noriega, S. Mehra, A. Salleo and A. Martucci, *J. Am. Chem. Soc.*, 2013, **135**, 3439-3448.
27. K. Manthiram and A. P. Alivisatos, *J. Am. Chem. Soc.*, 2012, **134**, 3995-3998.
28. K. Biswas and C. N. R. Rao, *J. Phys. Chem. B*, 2006, **110**, 842-845.
29. Q. Q. Huang, S. Hu, J. Zhuang and X. Wang, *Chem. Eur. J.*, 2012, **18**, 15283-15287.
30. T. R. Gordon, M. Cargnello, T. Paik, F. Mangolini, R. T. Weber, P. Fornasiero and C. B. Murray, *J. Am. Chem. Soc.*, 2012, **134**, 6751-6761.
31. A. Teleki and S. E. Pratsinis, *Phys. Chem. Chem. Phys.*, 2009, **11**, 3742-3747.
32. L. De Trizio, R. Buonsanti, A. M. Schimpf, A. Llordes, D. R. Gamelin, R. Simonutti and D. J. Milliron, *Chem. Mater.*, 2013, **25**, 3383-3390.
33. T. R. Gordon, T. Paik, D. R. Klein, G. V. Naik, H. Caglayan, A. Boltasseva and C. B. Murray, *Nano Lett.*, 2013, **13**, 2857-2863.
34. D. J. Rowe, J. S. Jeong, K. A. Mkhoyan and U. R. Kortshagen, *Nano Lett.*, 2013, **13**, 1317-1322.
35. L. M. Wheeler, N. R. Neale, T. Chen and U. R. Kortshagen, *Nat. Commun.*, 2013, **4**.
36. M. J. Polking, P. K. Jain, Y. Bekenstein, U. Banin, O. Millo, R. Ramesh and A. P. Alivisatos, *Phys. Rev. Lett.*, 2013, **111**.
37. M. Bruchez, M. Moronne, P. Gin, S. Weiss and A. P. Alivisatos, *Science*, 1998, **281**, 2013-2016.
38. X. H. Huang, I. H. El-Sayed, W. Qian and M. A. El-Sayed, *J. Am. Chem. Soc.*, 2006, **128**, 2115-2120.
39. X. M. Yang, S. E. Skrabalak, Z. Y. Li, Y. N. Xia and L. H. V. Wang, *Nano Lett.*, 2007, **7**, 3798-3802.
40. J. L. West and N. J. Halas, *Annu. Rev. Biomed. Eng.*, 2003, **5**, 285-292.
41. C. Kim, C. Favazza and L. H. V. Wang, *Chem. Rev.*, 2010, **110**, 2756-2782.
42. G. Ku, M. Zhou, S. L. Song, Q. Huang, J. Hazle and C. Li, *ACS Nano*, 2012, **6**, 7489-7496.
43. X. Liu, W. C. Law, M. Jeon, X. Wang, M. Liu, C. Kim, P. N. Prasad and M. T. Swihart, *Adv. Healthcare Mater.*, 2013, **2**, 952-957.
44. S. Lal, S. E. Clare and N. J. Halas, *Acc. Chem. Res.*, 2008, **41**, 1842-1851.
45. C. M. Hessel, V. P. Pattani, M. Rasch, M. G. Panthani, B. Koo, J. W. Tunnell and B. A. Korgel, *Nano Lett.*, 2011, **11**, 2560-2566.
46. Q. W. Tian, F. R. Jiang, R. J. Zou, Q. Liu, Z. G. Chen, M. F. Zhu, S. P. Yang, J. L. Wang, J. H. Wang and J. Q. Hu, *ACS Nano*, 2011, **5**, 9761-9771.
47. R. J. Mortimer, *Chem. Soc. Rev.*, 1997, **26**, 147-156.
48. A. Llordes, G. Garcia, J. Gazquez and D. J. Milliron, *Nature*, 2013, **500**, 323-326.
49. J. Lee, S. Lee, G. L. Li, M. A. Petruska, D. C. Paine and S. H. Sun, *J. Am. Chem. Soc.*, 2012, **134**, 13410-13414.
50. G. V. Naik, V. M. Shalaev and A. Boltasseva, *Adv. Mater.*, 2013, **25**, 3264-3294.

TOC Entry:

A new class of plasmonic nanomaterials, based upon heavily-doped semiconductors and metal oxides, is rapidly developing and showing great promise for biomedical and optoelectronic applications.